Supplementary Information

Hierarchical copper cobalt sulfide nanobelt arrays for high performance asymmetric supercapacitors

Leiyun Han [a], Xilong Liu [a], Zheng Cui [a], Yingjie Hua [b], Chongtai Wang [b*], Xudong Zhao [a*], Xiaoyang Liu [a, b*]

[a] State Key Laboratory of Inorganic Synthesis and Preparative Chemistry, College of Chemistry, Jilin University, Changchun, 130012, China

[b] Key Laboratory of Electrochemical Energy Storage and Energy Conversion of Hainan Province, School of Chemistry and Chemical Engineering, Hainan Normal University, Haikou, 571158, China

* E-mail: liuxy@jlu.edu.cn (XY Liu); oehy2014@163.com (CT Wang)

Table of contents

Materials and methods

Chemicals

The chemical reagents used in the experiments were all analytically pure and not further purified. Cobalt nitrate hexahydrate ($Co(NO_3)_2·6H_2O$), urea ((H_2NCONH_2), potassium hydroxide (KOH), ammonia ($NH_3·H_2O$), tetrapropyl orthosilicate (TPOS), formaldehyde (CH_2O), and resorcinol ($C_6H_6O_2$) were purchased from Sinopharm Chemical Reagent Co., Ltd. Copper nitrate trihydrate ($Cu(NO_3)_2·3H_2O$)and sodium sulfide ($Na_2S·9H_2O$) were purchased from Shanghai Macklin Biochemical Co., Ltd.

Synthesis of Cu-Co nanobelt arrays precursors on nickel foam

The preparation of Cu-Co nanobelt arrays precursors were completed by a simple one-step hydrothermal method. Prior to the experiments, nickel foam was cut into 1 × 3 cm^2 pieces, sonicated by ethanol and acetone for 30 min and cleaned with 3 mol L^{-1} HCl for 30 min to remove surface oxides, and finally washed with deionized water and dried in a vacuum oven at 80 °C. A typical process was as follows: 72.48 mg $Cu(NO_3)·3H_2O$, 174.62 mg $Co(NO_3)_2·6H_2O$, and 72.07 mg urea were dissolved in 30 mL deionized water by stirring for 15 min, and the solution was transferred to a 50 mL Teflon-lined autoclave and heated to 120°C for 8 h. After cooling down to room temperature, the samples were taken out and washed with deionized water and ethanol for 5 min., and dried in a vacuum oven at 80°C for 12 h. The final product can then be obtained. For the same process, different reaction times of 2 h, 4 h, 6 h, and 10 h were investigated. Similarly, the hydrothermal time was unchanged for 8 h. The effects of

different temperatures were further investigated under 100°C and 140°C, respectively.

Synthesis of $CuCo_2S_4$ nanobelt arrays on nickel foam

$CuCo_2S_4$ nanobelts were prepared via a secondary hydrothermal sulfidation method. The precursors of Cu-Co and 30 mL concentration of 10×10^{-3} mol L^{-1} Na_2S solution were added into a 50 mL Teflon-lined autoclave and kept at 120 ℃ for 6 h. After cooling to room temperature, the samples were taken out and ultrasonically cleaned with deionized water and ethanol for 5 min. and dried at 80 ℃ for 12 h. Final products can be obtained and marked as CCS-6t (t represents the reaction time). Similarly, experimental procedures were taken for the preparation of 4 h and 8 h electrode materials (denoted as CCS-4t and CCS-8t). In addition, sulfidation time was unchanged at 6 h and different Na_2S concentrations ranging from 5×10^{-3} mol L^{-1}, 10×10^{-3} mol L^{-1}, 20×10^{-3} mol L^{-1}, 30×10^{-3} mol L^{-1} (denoted as CCS-5M, CCS-10M, CCS-20M and CCS-30M, M represents concentrations) were used to further evaluate the effect of different concentrations of S^{2-}.

Synthesis of nitrogen-doped double-layer carbon hollow microspheres

For details of the preparation of nitrogen-doped double-layer carbon hollow microspheres (marked as N-DLCHs), see **Scheme 2** in Supporting Information. The typical synthesis processes were as follows: 7 mL of TPOS was added to a solution containing 140 mL of ethanol, 20 mL of deionized water, and 6 mL of $NH_3 \cdot H_2O$ at room temperature and stirred for 20 min. Next, 0.8 g resorcinol, and 1.2 mL formaldehyde solution were added to the above mixed solution and

stirred continuously for 24 h. The samples were collected by centrifugation and dried in a vacuum oven at 80°C for 12 h. The powder was carbonized in a tube furnace under argon atmosphere at 700°C for 3 h at a heating rate of 3°C/min to obtain a single-layer carbon hollow microspheres precursor, denoted as Pre-SLCHs. In addition, double-layer carbon hollow microspheres precursors were obtained by simply repeating the above process once prior to centrifugation collection and stirring continuously for another 24 h, the same calcination steps as Pre-SLCMs were performed and denoted as Pre-DLCHs.

Finally, 0.5 g Pre-DLCHs was added to 20 mL of methanol solution containing 0.3 g of melamine and stirred at 70°C until the methanol completely evaporated. The mixture was carbonized for 3 h under argon atmosphere at a heating rate of 3°C/min. in tube furnace at 700°C. After calcination, the powder was collected and soaked in HF (10 wt.%) for 6 h to remove the SiO_2 colloidal core, collected by centrifugation and dried in a vacuum oven at 80°C for 12 h to obtain N-DLCHs. The materials were formed under the same way to obtain N-SLCHs.

Assembly of asymmetric supercapacitors

To further demonstrate the electrochemical performance and practical applications of the samples, asymmetric superconductors (SCs) with a sandwich structure (positive/separator/negative) were assembled using $CuCo_2S_4$ nanobelt arrays as the positive, N-DLCHs as the negative, glass fiber paper as the separator, and 6 mol L^{-1} KOH as the electrolyte. In asymmetric SCs, the two

electrodes have different specific capacitances, masses and potential windows. In order to construct asymmetric SCs, a charge balance relationship： $Q^+ = Q^-$， should be followed between the positive and negative electrodes, where the charge stored by the positive and negative electrodes depends on the specific capacity (C), the potential range of the discharge process (ΔV) and the mass of the electrodes (m), following the below equation [54]:

$$Q^+ = Q^- \#(4)$$

$$Q = C \times \Delta V \times m \#(5)$$

$$C^+ \times \Delta V^+ \times m^+ = C^- \times \Delta V^- \times m^- \#(6)$$

Thus, calculations based on GCD curves at 1 A g^{-1} showed that the $CuCo_2S_4$ electrode specific capacity was about 1014 C g^{-1} (equivalent to 1988 F g^{-1}, **Fig. 4(d-e)**), and the specific capacity/capacitance of N-DLCHs was 230 C g^{-1} / F g^{-1} (the potential window is 1 V, in **Fig. 5(e)**) at 1 A g^{-1}. In this work, the loading mass of active materials was 2.2 ± 0.3 mg for $CuCo_2S_4$ (more details about the mass loading of active material see Table S3), thus, the loading mass ratio of active materials ($CuCo_2S_4$/N-DLCHs) was estimated to be 0.22, the negative N-DLCHs loading was about 10 mg and the whole device loading was about 12 mg.

Materials characterization

The morphologies and structures of the samples were characterized by scanning electron microscopy (FE-SEM, JEOL JSM 6700F) and transmission electron microscopy (FEI Tecnai G2 S-Twin F20 D573). The crystal structure of the materials was analyzed by X-ray diffraction (XRD, D/max 2550V/PC, CuKα

radiation), and surface elemental analysis. Oxidation states were characterized by X-ray photoelectron spectroscopy (XPS, ESCALAB 250, Mg Kα radiation) and energy dispersive X-ray spectroscopy (EDS, FEI Helios Nanolab 600i), and the specific surface area and pore size distribution results were obtained by specific surface area analyzer (ASAP 2420).

Electrochemical measurements

Electrochemical measurements were performed on an electrochemical workstation (CHI760e, CH Instruments Inc., Shanghai) in 6 mol L^{-1} KOH. A standard three-electrode system was used, with $CuCo_2S_4$ as the working electrode, Pt foil as the counter electrode, Hg/HgO electrode as the reference electrode. The asymmetric device was investigated using a two-electrode testing cell. The N-DLCHs negative was prepared by grinding a mixture of active material, acetylene black and PTFE in a mass ratio of 8:1:1, and pressed onto a nickel foam under 3 MPa. The average mass loading of N-DLCHs was 3.5 ± 0.5 mg. Cyclic voltammetry (CV) curves were performed at different scan rates from 10-100 mV s^{-1} in the potential range of 0.0-0.6 V and -1-0 V. Galvanostatic charge/discharge (GCD) curves were performed at different current densities in the voltage range 0.0-0.6 V and -1-0 V. Electrochemical impedance spectroscopy (EIS) was performed at an AC voltage of 5 mV amplitude applied in the frequency range 0.01-100 kHz.

The mass specific capacity ($\boldsymbol{C_m}$), area specific capacity ($\boldsymbol{C_s}$), energy density ($\boldsymbol{E}$) and power density ($\boldsymbol{P}$) of the electrodes and devices are calculated by the

following equations [1]:

$$C_m = \frac{i \times \Delta t}{m} \#(7)$$

$$C_s = \frac{i \times \Delta t}{S} \#(8)$$

$$E = \frac{1}{2} \times C \times (\Delta V)^2 \#(9)$$

$$P = \frac{E}{\Delta t} \#(10)$$

where C_m (C g^{-1}) is the mass specific capacity, C_s is the area specific capacity (C cm^{-2}), i (A) is the charge/discharge current, Δt (s) is the discharge time, ΔV (V) is the discharge potential window, S (cm^{-2}) is the test electrode area, and m (g) is the electrode active mass loading.

Characterization of Cu-Co nanobelt arrays precursors

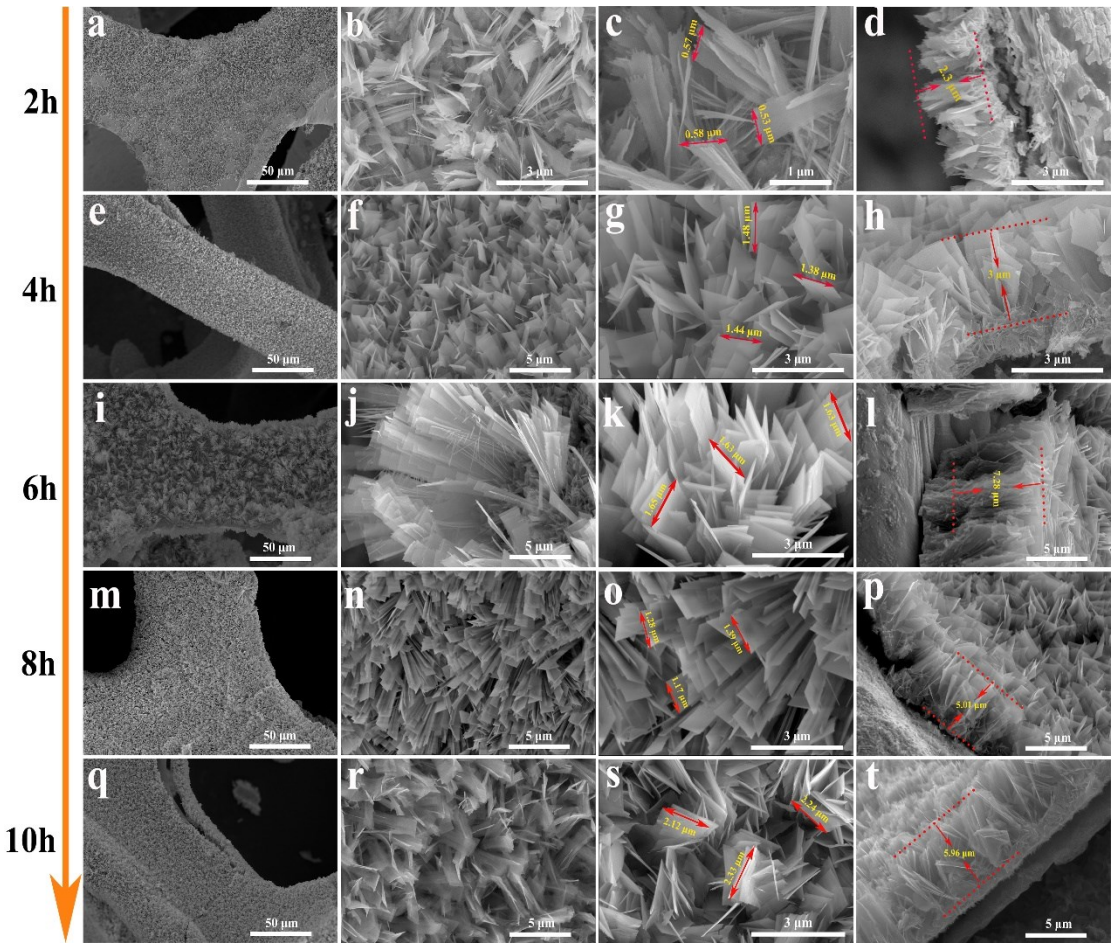

Figure S1: SEM images of Cu-Co nanobelt array precursor electrodes obtained via the hydrothermal reactions under different times: (a-d) 2 h, (e-h) 4 h, (i-l) 6 h, (m-p) 8 h, and (q-t) 10 h.

In order to investigate the evolution in the formation of Cu-Co precursors on nickel foam substrates (NFs), a detailed study was carried out by adjusting reaction times. The morphology changes of the samples shown in **Fig. S1** revealed the important influence of different reaction times at 120 °C on the microstructure of Cu-Co nanobelt precursors. In the initial 0-2 h, thin nanobelt

structures interlaced and appeared on the NFs, but due to the short reaction time, the copper-cobalt salt solution could not react completely, and the NFs had large exposed parts, while the nanobelt flakes grew sparsely and disorderly, as shown in **Fig. S1(a, b)**. At the same time, in **Fig. S1(c, d)**, the surface was rough, and they piled up on each other. The length of the nanobelt was about 2.3 um and the width average were about 0.55 um. With the time up to 4 h, it was clear from **Fig. S1(e, f)** that the nanobelts became dense, the exposed parts of the NFs decreased, and the nanobelts were independent of each other in a staggered arrangement, the surface was relatively smooth, and the overlap phenomenon was reduced. At this time, the length and width of the nanobelts increased significantly, as shown in **Fig. S1(g, h)**, the length was about 3 um and the width average were 1.43 um. When the time was increased to 6 h, as depicted in **Fig. S1(i-l)**, the precursors were evenly coated on the NFs, and the surface of the skeleton was regular as a whole, at which time the nanobelts loading density increased rapidly, and the length of the nanobelts increased to 7.28 um and the width average was about 1.64 um. Due to the increased density of the nanobelts, the distance between them became smaller and partial stacking occurred. Upon extending the time to 8 h, in Fig. **S1(m, n)**, the nanobelts were aligned regularly on the NFs, with a smooth surface and complete structure, with no accumulation between them. In addition, the length and width of the nanobelts were significantly reduced to about 5.01um and 1.28 um respectively, as shown in Fig. **S1(o, p)**. Due to the sufficient growth at the appropriate reaction time and the

fine adjustment of the axial structure, resulting in the decrease of the length and width. This improved the mechanical stability of the microstructure, which was beneficial to the electrochemical cycle stability process. As the time increased to 10 h as shown in Fig. **S1(q, r),** the precursors still maintained the nanobelt morphology, but the structures were crushed in a large area. This may be because the over growth caused the nanobelt loading continue to increase, which leaded to the collapse of the morphology. Meanwhile, as shown in **Fig. S1(s, t)**, the length and width were about 5.96 um and 2.23 um, respectively. From the initial to 8 h, the increase in reaction time played a positive effect on the formation of nanobelts, which gradually increased in length and width. After 8 h, the excessive reaction time had a negative effect on the formation of the nanobelts and prevented their further growth and compromised their structural integrity. Meanwhile, time had more influence on the axial length and width of the nanobelt formation process, while the effect on the thickness was not obvious. Therefore, the optimal reaction time of Cu-Co nanobelt precursors should be controlled at 8 h at the reaction temperature of 120°C.

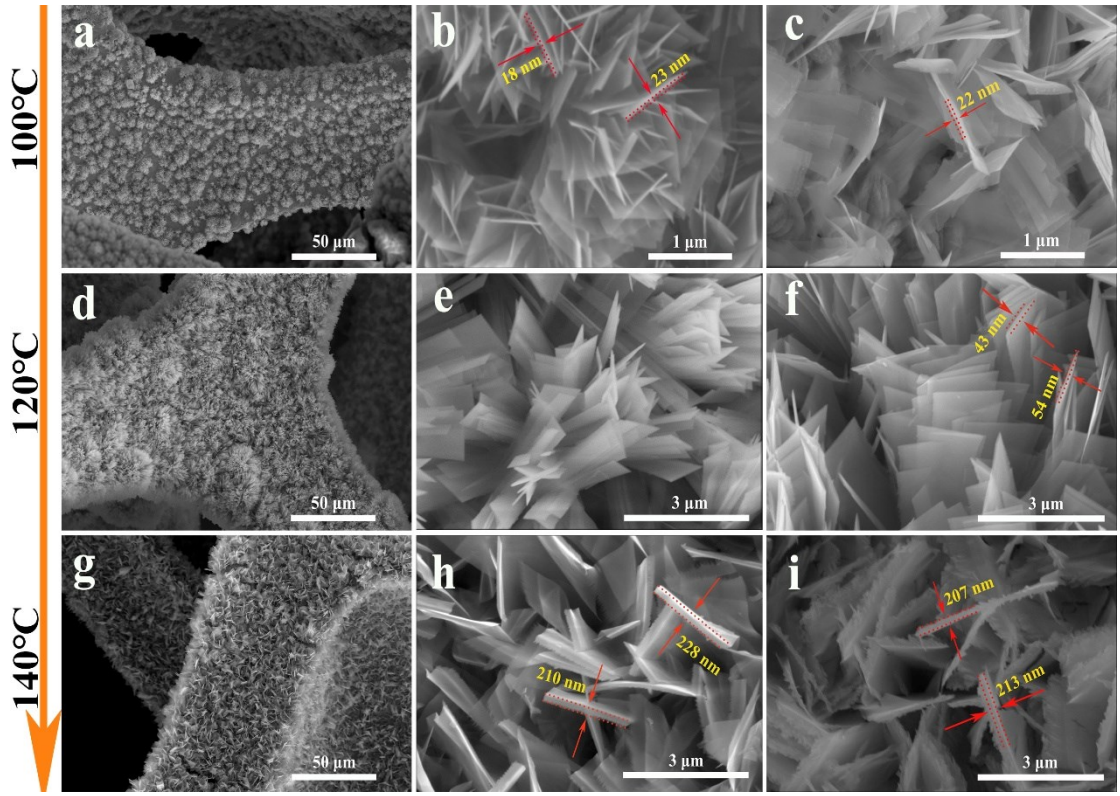

Figure S2: SEM images of Cu-Co nanobelt array precursor electrodes obtained via the hydrothermal reaction under different temperatures: (a-c) 100℃, (d-f) 120℃, and (g-i) 140℃。

On the other hand, the hydrothermal temperature is factor that cannot be ignored. Under the optimal reaction time of 8 h, by adjusting the reaction temperature, the microscopic changes of the nanobelts morphology at different temperatures are further discussed. At a lower reaction temperature of 100℃, as revealed in **Fig. S2(a)**, there was an accumulation of small clusters on the NFs, the NFs were severely exposed. Through further enlargement of the image in **Fig. S2(b)**, these clusters were formed by a piece of incomplete growth of the "transition state" of the nanobelt flakes, and at this time the nanobelts were disorderly. This may be due to the incomplete reaction between the copper-cobalt salt solution and the precipitant urea at low temperature and partial deposition

on the NFs, and the fact that low temperature was not beneficial for the vertical growth of nanobelts, resulting in severe agglomeration with each other. The thickness of the nanobelts was in the range of about 21 nm, as shown in **Fig. S2(c).** When the temperature was increased to 120℃, from the **Fig. S2(d, e)**, the NFs were completely covered by the nanobelts, the surface was regular, the morphology was most complete and the aspect ratio was obvious. In **Fig. S2(f)**, the thickness of the nanobelts had increased significantly compared to 100°C under high magnification. Its value was measured to be between 48~55 nm. As the reaction was further increased to 140°C, the morphology of the nanobelts remained unchanged, but the thickness had increased significantly compared to others under high magnification, as shown in **Fig. S2(h, i)**, which was approximately between 200~230 nm. It was possible that the high temperature increased the kinetics of the reaction faster and accelerated the nucleation growth of the precursors, such that the growth of the nanobelts were rapid and uncontrolled [41]. As a result, the thickness of the nanobelt increased significantly while the structural stability decreased. From the above results, it can be seen that the reaction temperature had an important effect on the thickness of the nanobelt, and the effect of temperature was more obvious and dominant than the effect of different reaction times on the thickness. As the reaction temperature increased, the thickness of the nanobelt gradually increased and became more and more obvious. At temperatures below 120°C, the nanobelt growth did not fully proceed and the substrate loading were low, which would greatly affect the

subsequent electrochemical properties. If the temperature exceeded 120℃, the high temperature would destroy the morphological and structural integrity of the nanobelt. Meanwhile, the thick nanobelt structure formed at the high temperature would be unfavorable to the infiltration of the electrolyte and reduce the contact area, which would be a serious obstacle to the improvement of the electrochemical properties. Therefore, the optimal reaction temperature of Cu-Co nanobelt precursors should be controlled at 120 °C.

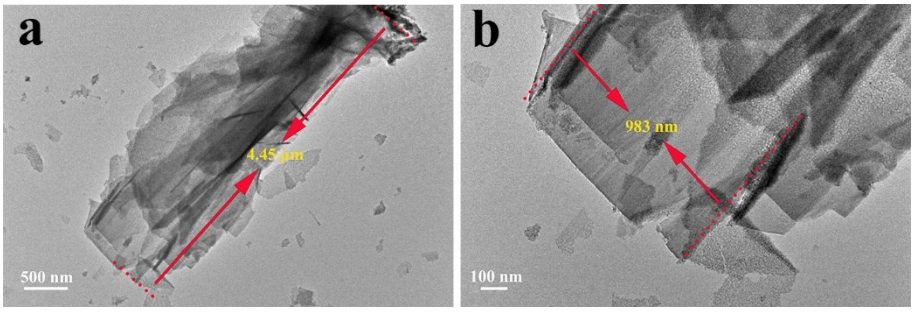

Figure S3: (a, b) Transmission electron microscopy (TEM) of Cu-Co precursors obtained under optimal conditions.

TEM images in **Fig. S3** also demonstrated the morphology and nanostructure of Cu-Co precursors. It can be seen that the length of the nanobelts was about 4.45 μm and the width was about 983 nm, as depicted in **Fig. S3(a, b)**, which matched the results observed in the SEM.

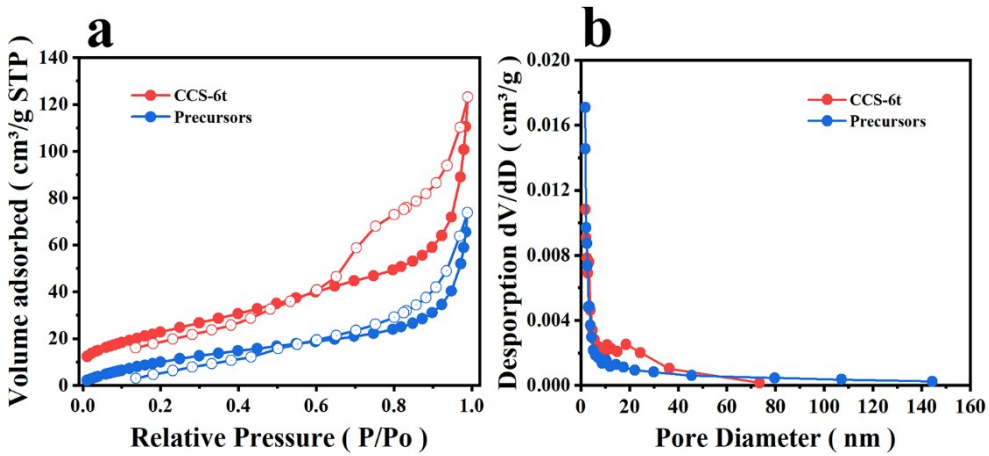

Figure S4： (a) The N_2 adsorption-desorption isotherm of precursors and corresponding optimal $CuCo_2S_4$, (b) Pore-size distribution curve as obtained from the BJH method.

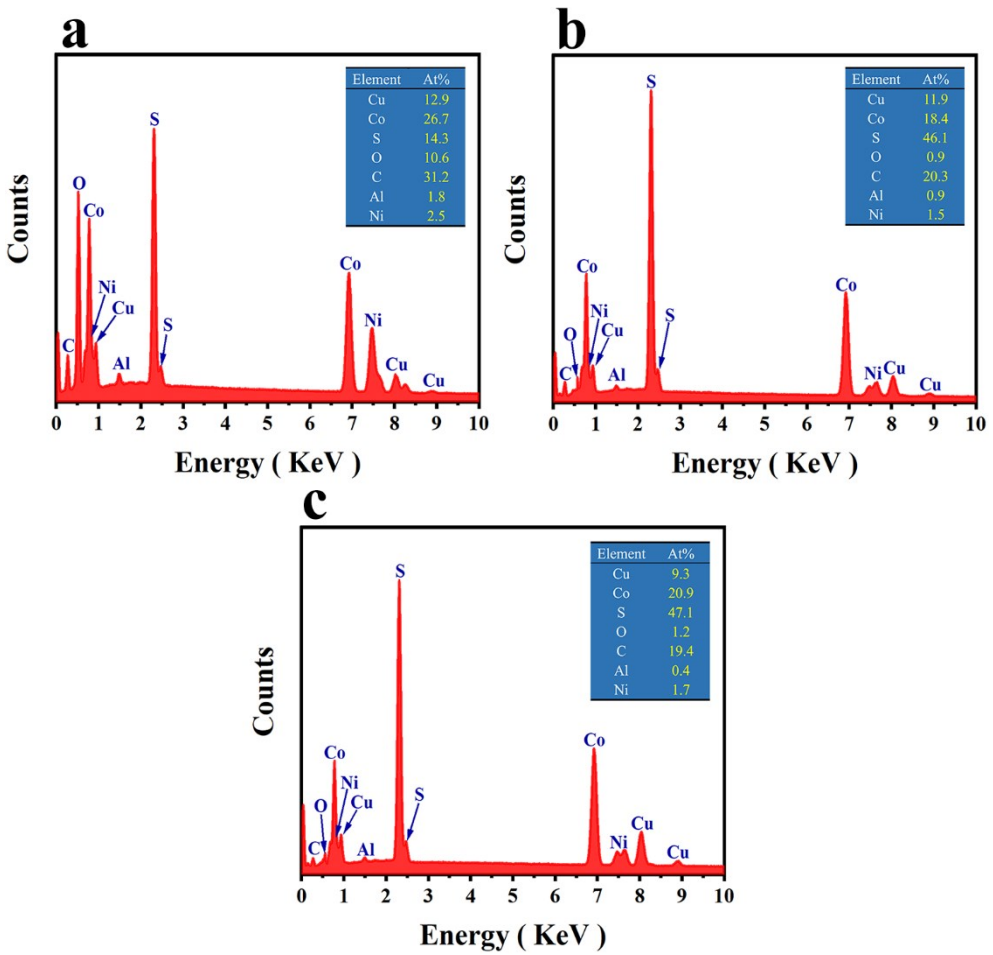

Figure S5: EDS patterns of the Cu-Co sulfides obtained with different C_S^{2-} of (a) 5 mM, (b) 20 mM, and (c) 30 mM.

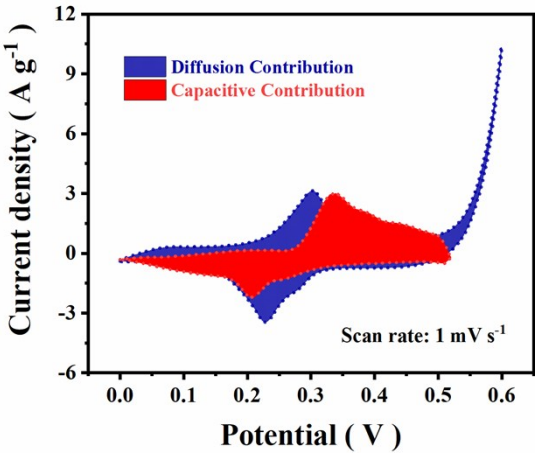

Figure S6: Capacitive and diffusion-controlled charge storage contributions at the scan rate of 1.0 mV s^{-1}.

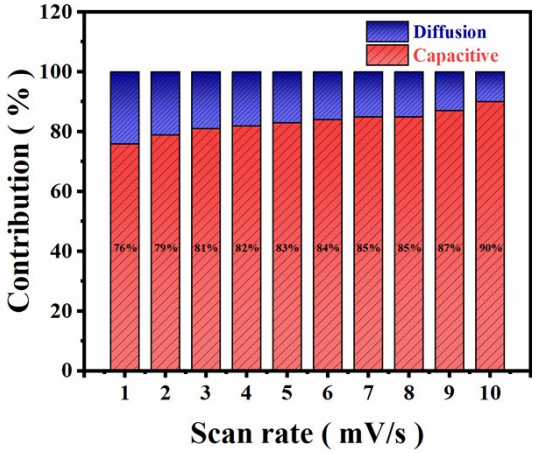

Figure S7: The contribution ratio of capacitive and diffusion-controlled charge storage at various scan rates ranging from 1 to 10 mV s^{-1}.

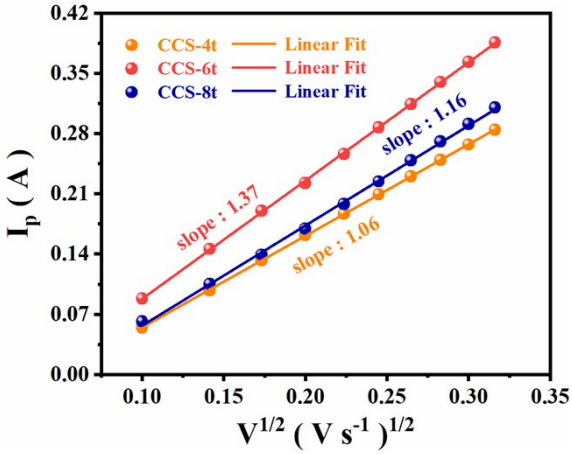

Figure S8: The linear fitting of peak currents versus $v^{1/2}$ of different C_s^{2-}.

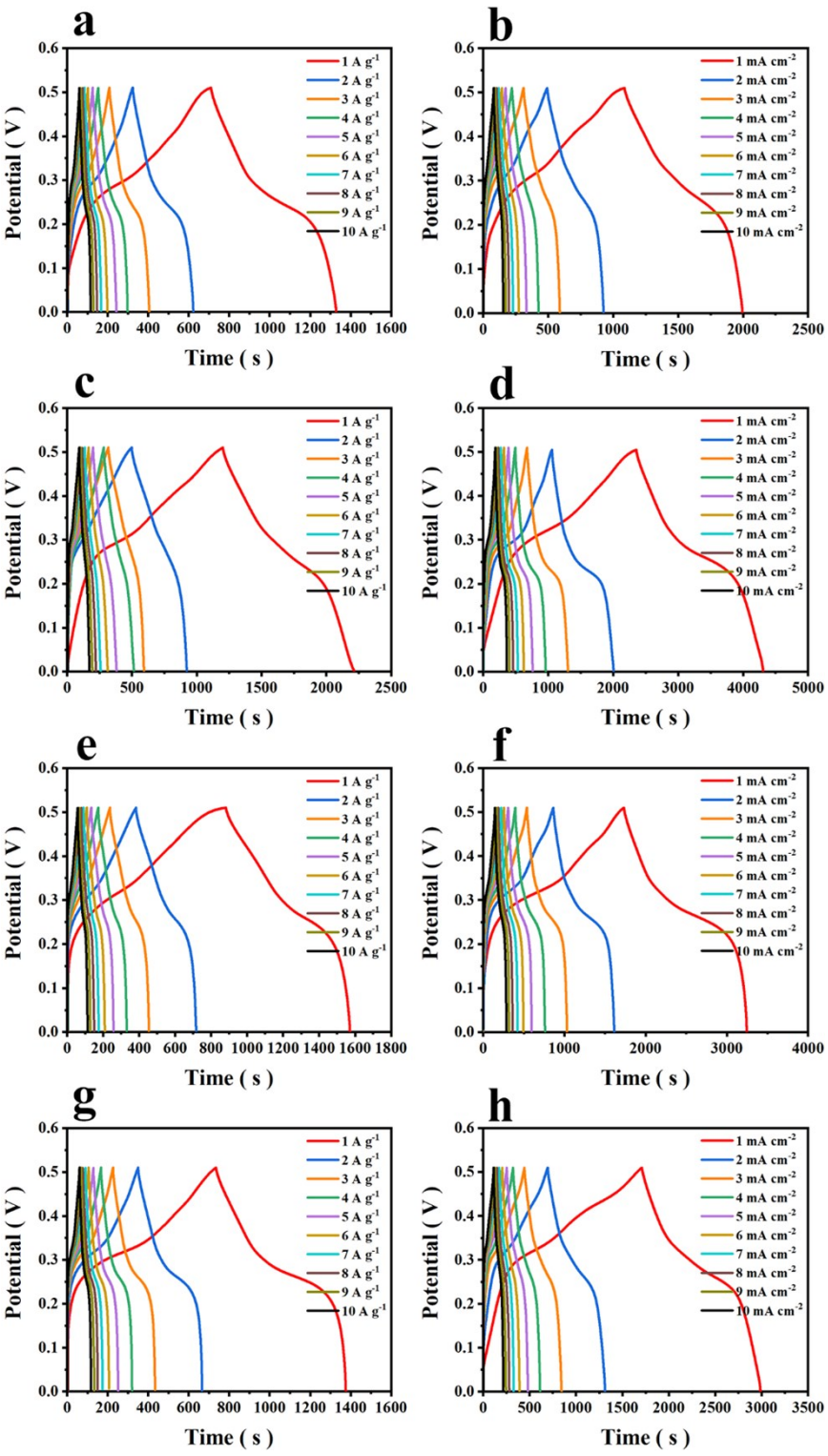

Figure S9: GCD tests of the samples obtain at different C_s^{2-}: (a, b) 5mM, (c, d) 10mM, (e, f) 20mM, and (g, h) 30mM.

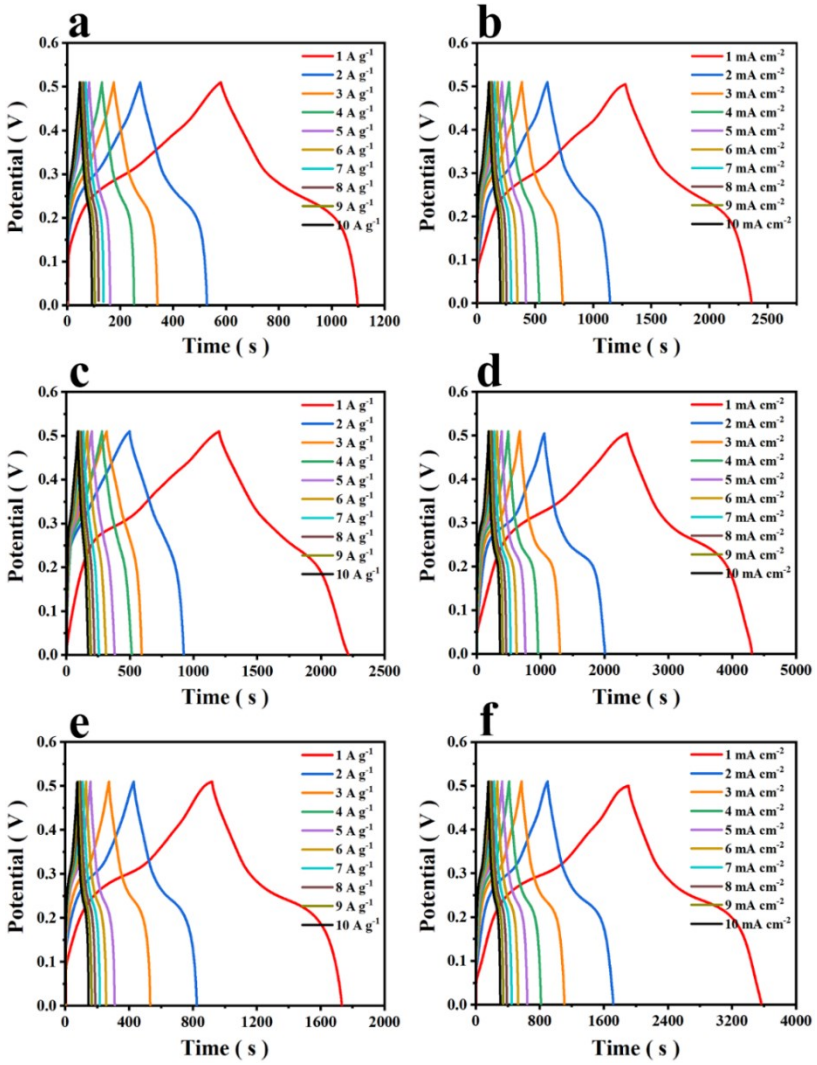

Figure S10: GCD tests of the samples obtain at different reaction times: (a, b) 4 h, (c, d) 6 h, and (e, f) 8 h.

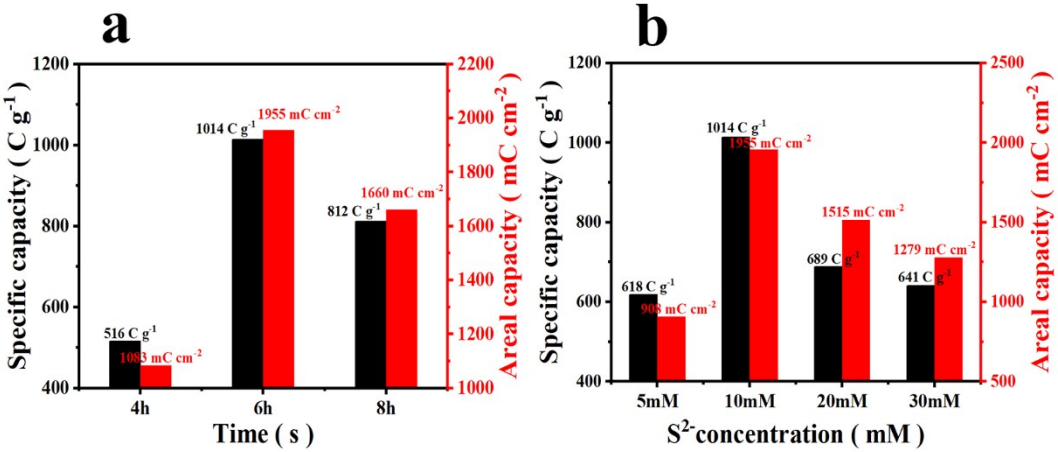

Figure S11: Calculation of specific capacity at 1 A g^{-1} of the samples obtain at different reaction times and C_s^{2-} by GCD test.

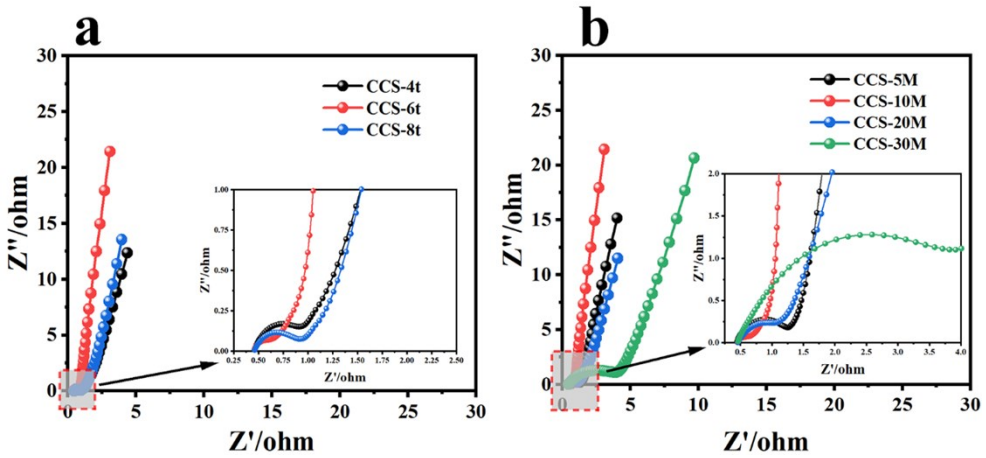

Figure S12: Nyquist plots of the $CuCo_2S_4$ nanobelt arrays electrode obtain at different reaction times and C_s^{2-}.

Electrochemical impedance spectroscopy tests were conducted to further characterize the resistance and capacitance properties of the electrodes. **Fig. S12(a, b)** and enlarged insets showed Nyquist plots of the $CuCo_2S_4$ nanobelts obtained at different reaction times and C_s^{2-}. The Nyquist plots of all electrodes showed a semicircle in the high frequency region and an approximate straight line in the low frequency region. The semicircle at high frequency corresponds to the Faraday charge transfer resistance (R_{ct}), while the straight line represents the Warburg impedance, which shows the diffusion of electrolytes and protons in the active material [S1]. In addition, the intersection of the high frequency with the coordinate axis represents the resistance (R_s) of the system, including the internal resistance of the electrolyte and the electrode. The CCS-6t and CCS-10M electrodes had the lowest R_{ct} and R_s, according to the fitting process of Zview 2.0 platform, at 0.46 Ω and 0.24 Ω, respectively.

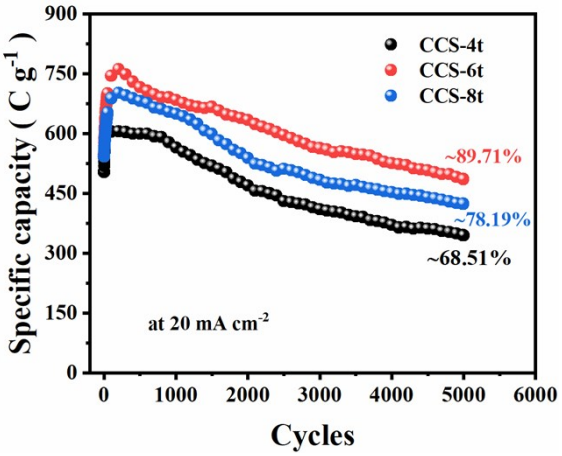

Figure S13: Cycle stability of $CuCo_2S_4$ electrodes over 5000 cycles at 20 mA cm^{-2} obtain at different reaction times.

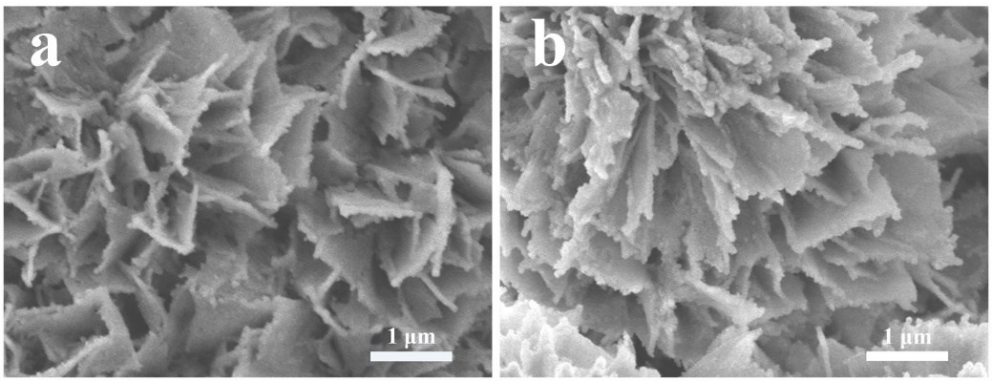

Figure S14： The SEM of CCS-10M electrodes after 5000 cycles of charge and discharge test.

After 5000 cycles of charge and discharge tests, the morphology and structure of the nanobelts were relatively intact, and the thickness of the nanobelts increased slightly after the cycle compared with the initial electrode, which may be caused by the volume expansion of the material during the long-time charge/discharge process under high current density.

Characterization of nitrogen-doped double-layer carbon hollow microspheres

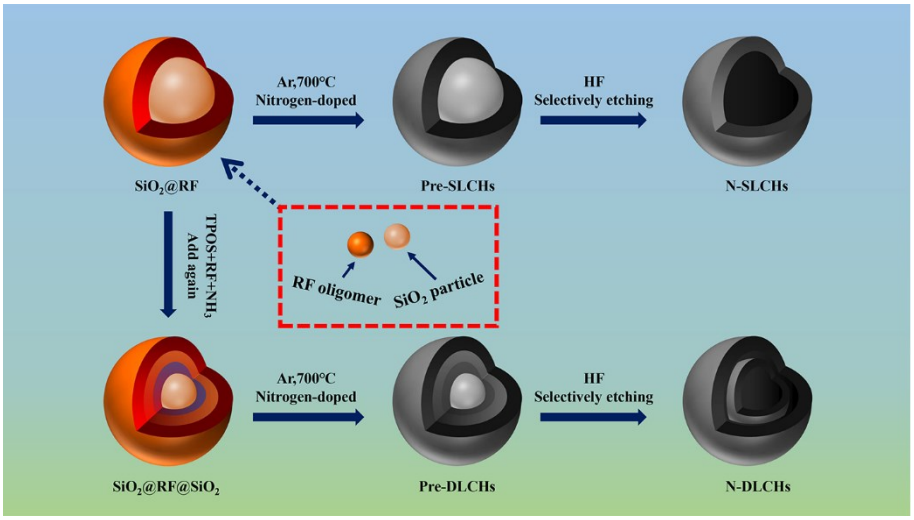

Scheme 2. Schematic illustration of the synthesis procedure of the nitrogen-doped single/double-layer carbon hollow microspheres.

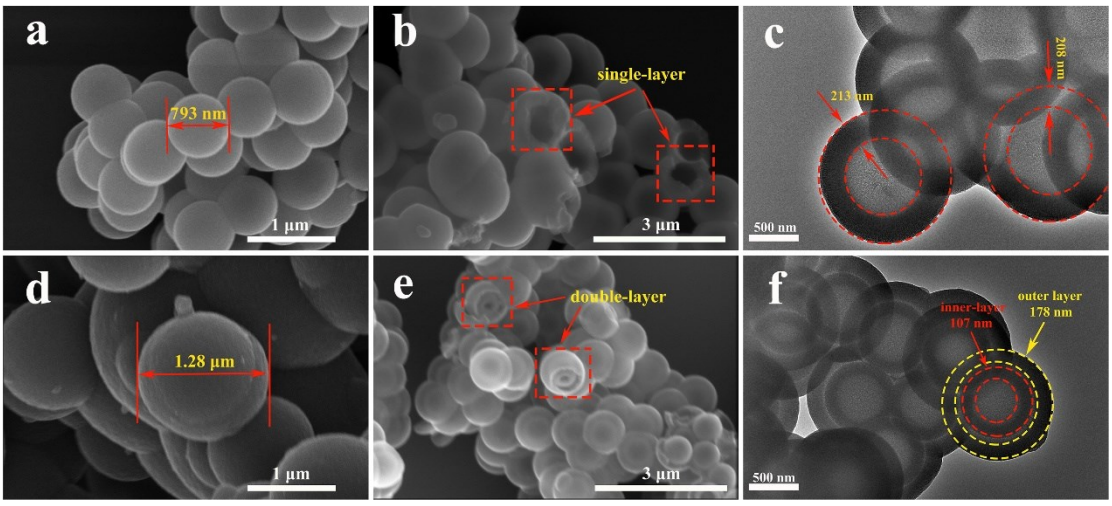

Figure S15: Morphological characterizations: (a, b) low- and high-magnification SEM images of N-SLCHs, (c) high resolution TEM images of N-SLCHs, (d, e) low- and high-magnification SEM images of N-DLCHs, and (f) high resolution TEM images of N-DLCHs.

It was seen in **Fig. S15(d)** that N-DLCHs had a relatively large diameter

with a value of 1.28 um compared to N-SLCHs in **Fig. S15(a)**. The double-layer hollow structure can be seen in **Fig. S15(e)**, and this hollow structure was further evidenced in TEM images in **Fig. S15(f)**, while the double-layer structure had a thickness of about 107 nm for the inner-layer and about 178 nm for the outer-layer.

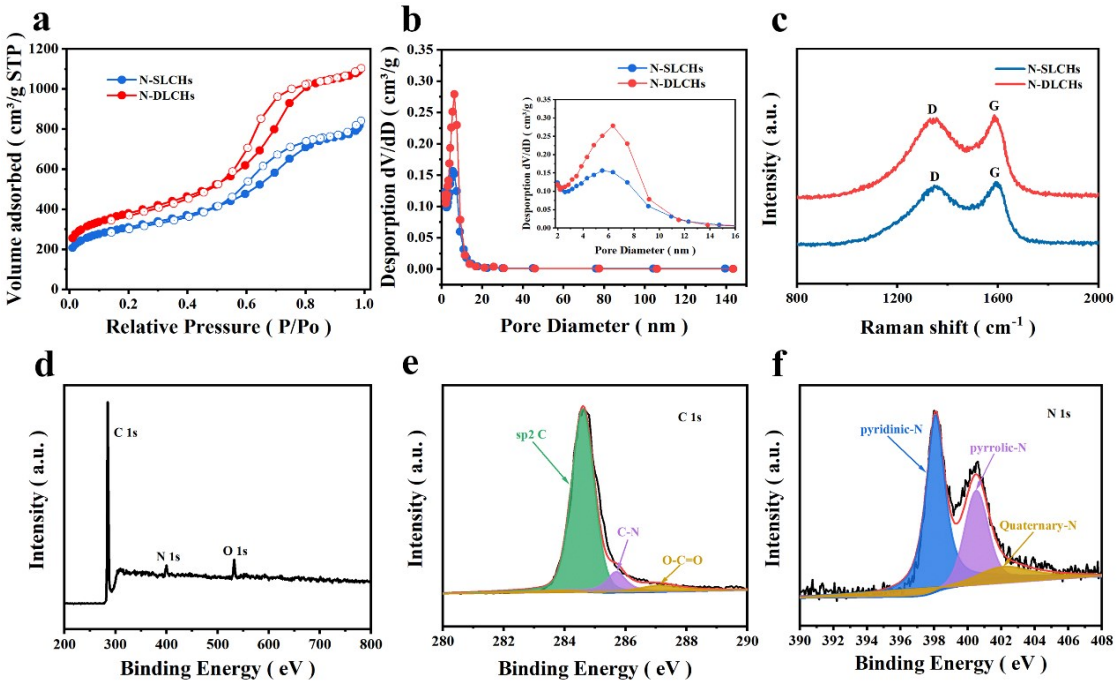

Figure S16: Pore structure characterization (a) N_2 adsorption/desorption isotherms, (b) Pore size distributions, (c) Raman spectra of N-SLCHs and N-DLCHs, (d) XPS survey spectrum of N-DLCHs, (e) C 1s, and (f) N 1s.

The N_2 adsorption-desorption isotherms and pore size distribution of N-DLCHs and N-SLCHs were shown in **Fig. S16(a)** and **(b)**. The N-DLCHs exhibited high surface areas of 1322.43 $m^2 g^{-1}$, but the surface areas of N-SLCHs were only 1048.37 $m^2 g^{-1}$. Furthermore, the pore size distribution in **Fig. 16(b)** was calculated by the Barrett-Joyner-Halenda (BJH) method. The calculation

confirmed that most of the pores were about 7 nm. The Raman spectra in **Fig. S16(c)** show D band at 1335.4 cm^{-1} and G band at 1583.34 cm^{-1}. The intensity ratio of D-band and G-band (I_D/I_G) was 0.965 for N-SLCHs, 0.981 for N-DLCHs, suggesting that nitrogen-doped multi-layer carbon microspheres possess similar carbon microstructures due to their identical preparation method [53].

The elemental composition of the N-DLCHs was further investigated by X-ray photoelectron spectroscopy (XPS) as shown in **Fig. S16(d-f)**. The presence of C, N, and O elements were confirmed by the survey spectrum in **Fig. S16(d)**, where the C, N, and O contents were 89.26%, 6.58%, and 4.16%, respectively. The XPS for C 1s as shown in **Fig. S16(e)**, N-DLCHs showed an obvious characteristic peak of C-N at 285.8 eV. The presence of C-N in the C 1s spectrum suggested successful doping of nitrogen in N-DLCHs. The N 1s spectrum exhibited three peaks at a binding energy of 398.6, 401.2 and 402.3 eV, **Fig. S16(f)**, corresponding to the pyridinic-N, pyrrolic-N, and Quatemary-N, respectively [S2]. These results further confirm that the nitrogen heteroatoms have been successfully doped into the N-DLCHs structure.

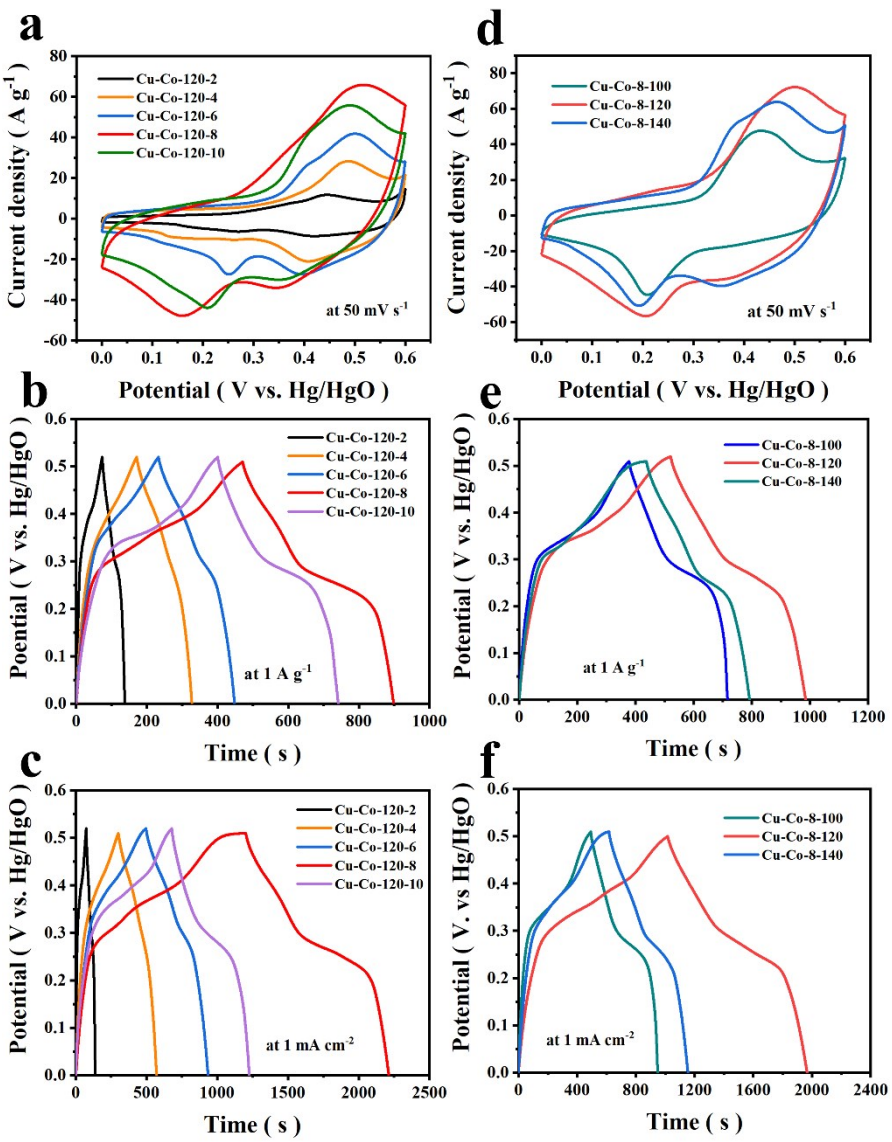

Figure S17： Electrochemical performances of Cu-Co precursor electrodes in aqueous electrolyte: (a-c) comparative CV and GCD curves of the precursor samples obtained at different reaction times, (d-f) comparative CV and GCD curves of the precursor samples obtained at different reaction temperature.

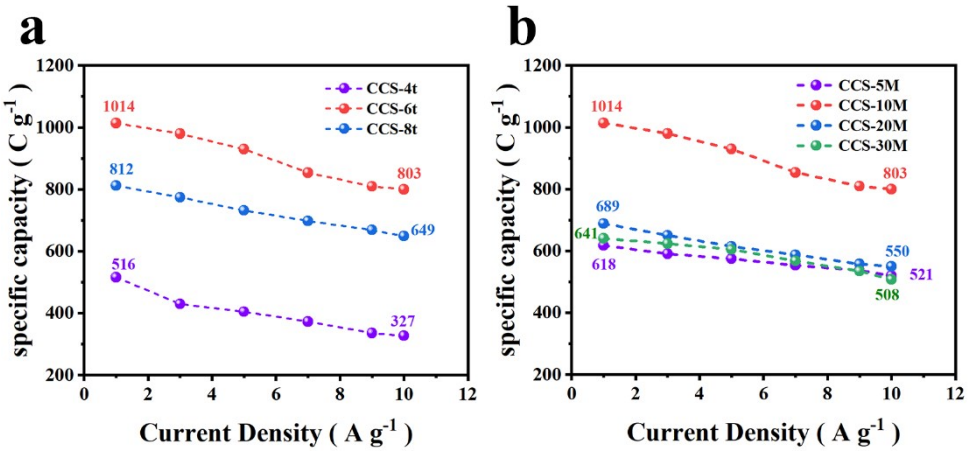

Figure S18. Rate capability of the CCS electrodes: (a) CCS electrodes obtained at different sulfidation reaction times, (b) CCS electrodes obtained at different C_s^{2-}.

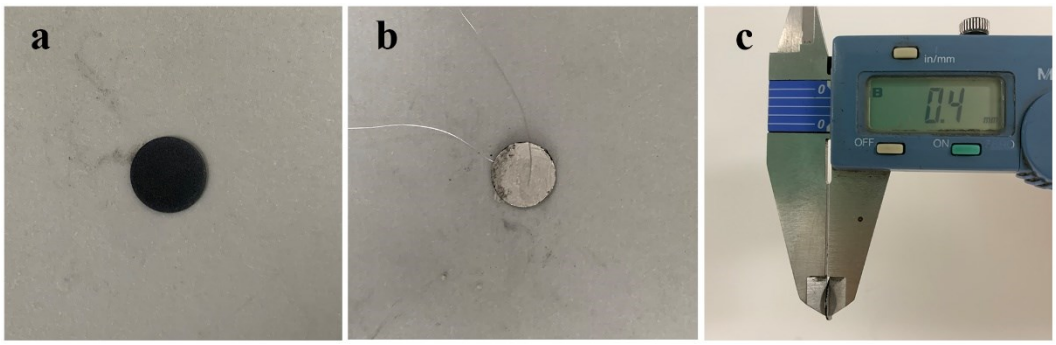

Figure S19. Photographs of the sample's preparation for conductivity test.

In order to obtain the results of electrical conductivity data, the experiments were performed as follows: the prepared material was scraped from the nickel foam with a knife, and the powder samples were collected and pressed at room temperature with a pressure of 10 MPa to form a disc with a diameter of 1 cm, as shown in **Fig. S19(a)**, and the pressing time was 10 min. After that, the both sides were evenly coated with conductive silver adhesives and fastened with silver wire, as shown in **Fig. S19(b)**. Finally, the thickness was measured by vernier caliper as 0.4 mm, as shown in **Fig. S19(c)**. The $\boldsymbol{\sigma}$ value was tested in two-electrode system on the Solartron 1260 + 1287 platform (Solartron Metrology, Co., Ltd, U.K.). To ensure the accuracy of the results, the tests were conducted at different stable potentials of 0.25V, 0.35V, and 0.45V. The final results were average values and $\boldsymbol{\sigma}$ values were calculated as given by the following equation:

$$R = \rho \times \frac{L}{S} \#(11)$$

$$\sigma = \frac{1}{\rho} \#(12)$$

where $\boldsymbol{R}$ (Ω) is the electronic resistance at the corresponding constant potentials, $\boldsymbol{\rho}$ (Ω cm) is the resistivity, $\boldsymbol{L}$ (cm) is the thickness of the material, $\boldsymbol{S}$ (cm^2) is the area of the material, and $\boldsymbol{\sigma}$ (S/cm) is the electrical conductivity. The results were shown in **Fig. S20** and **Table S4**.

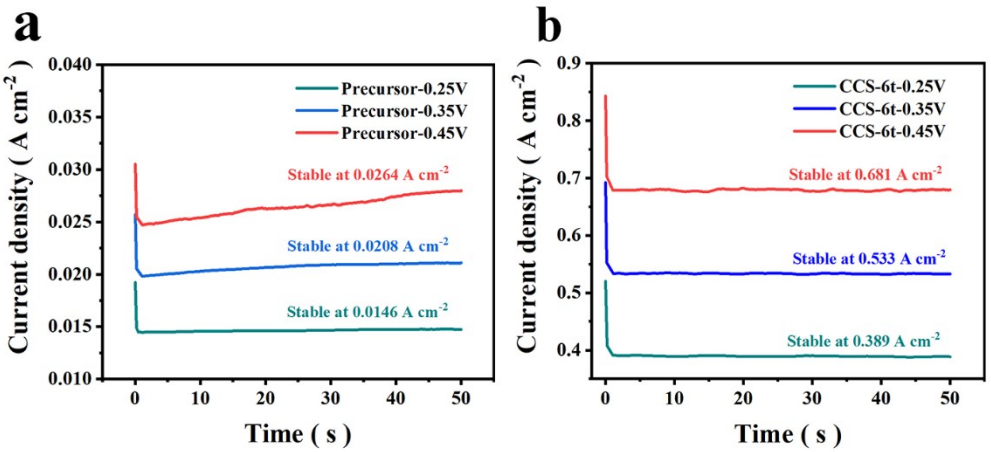

Figure S20. Conductivity tests at different potentials: (a) Precursors, (b) CCS-6t sample.

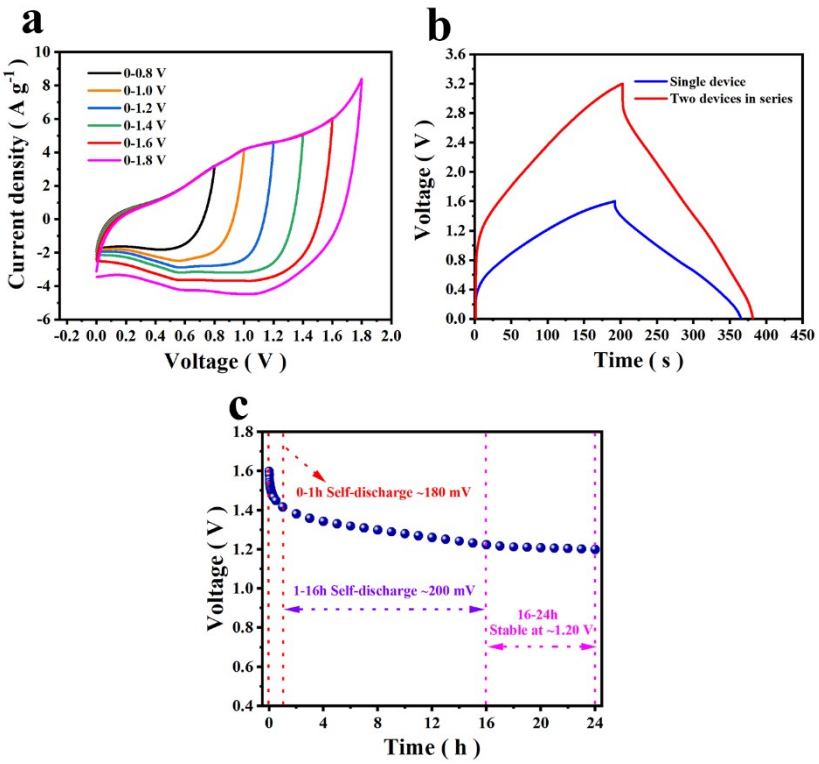

Figure S21. Electrochemical performance of N-DLCHs// $CuCo_2S_4$ asymmetric device: (a) CV curves of the device measured in different potential ranges, (b) two devices in series, and (c) self-discharge curve of the asymmetric device.

Table S1. Comparisons of the diffusion rates ($D_{K+/OH-}$, $cm^2\ s^{-1}$) of various electrodes under different conditions

Sample	$D_{K+/OH-}$
CCS-4t	3.38×10^{-10}
CCS-6t	$\mathbf{7.57\times10^{-10}}$
CCS-8t	4.62×10^{-10}
CCS-5M	3.78×10^{-10}
CCS-10M	$\mathbf{8.39\times10^{-10}}$
CCS-20M	6.41×10^{-10}
CCS-30M	6.03×10^{-10}

Table S2. Comparisons of CCS electrodes and supercapacitors devices performance with previous work.

Electrode	3E @current density	Cell	cycles	retention	ΔV (V)	ED (Wh kg^{-1})	Ref.
$CuCo_2S_4$-rGO microflowers	1280.2 F g^{-1} 1 A g^{-1}	2E, Sym.	3000	78.64% 5 A g^{-1}	1	16.1	35
flower-like $CuCo_2S_4$	908.9 F g^{-1} 5 mA cm^{-2}	2E, AC	2000	126.39 25 mA cm^{-2}	1.5	29.2	57
$Ni(OH)_2/CuCo_2S_4$/ Ni	749.13μA h cm^{-2} 1 mA cm^{-2}	2E, AC	5000	88% 6 A g^{-1}	1.45	39.7	44
$CuCo_2S_4$ hollow spheres	1137.5 F g^{-1} 2 A g^{-1}	3E	6000	94.9% 5 A g^{-1}	0.5	---	S3
mesoporous $CuCo_2S_4$	752 F g^{-1} 2 A g^{-1}	3E	5000	98.1% 3 A g^{-1}	0.5	---	S4
$CuCo_2S_4$/CNT /graphene	504 F g^{-1} 10 A g^{-1}	3E	2000	92.3% 20 A g^{-1}	0.4	---	S5
$CuCo_2S_4$/graphene	525.4 F g^{-1} 1A g^{-1}	3E	1000	82.7% 4 A g^{-1}	0.5	---	S6
$CuCo_2S_4$ nanosheet	3132.7 F g^{-1} 1A g^{-1}	2E, AC	4000	70.8% 2 A g^{-1}	1.8	46.1	33
$CuCo_2S_4$ nanorod arrays	1536.9 F g^{-1} 1 A g^{-1}	2E, AC	5000	88% 10 mA cm^{-2}	1.6	56.9	S7
$CuCo_2S_4$ hollow nanoneedle	6.5 F cm^{-2} 6 mA cm^{-2}	2E, AC	6000	94.1% 48 mA cm^{-2}	1.6	44.1	42
$CuCo_2O_4$@NiO nanowire	2.3 F cm^{-2} 2 mA cm^{-2}	2E, AC	6000	81.3% 50 mV s^{-1}	1.5	38.9	24
$CuCo_2S_4/CuCo_2O_4$ nanoflower	599.9 C g^{-1} 1 A g^{-1}	2E, GA	10,000	73% 20 A g^{-1}	1.6	33.2	34
$CuCo_2O_4$/CuO	642 F g^{-1} 1 A g^{-1}	2E, Fe_2O_3	5000	83% 5 A g^{-1}	1.6	33	58
$CuCo_2O_4$@$Co(OH)_2$	424 F g^{-1} 0.5 A g^{-1}	2E, AG	---	---	1.4	19.2	59
$CuCo_2O_4$/CuO particles	781 F g^{-1} 2 mV s^{-1}	2E, AC	5000	100% 5mA cm^{-2}	1.5	18	56
$CuCo_2O_4$ nano grasses	796 F g^{-1} 2 A g^{-1}	3E	5000	94.7% 2 A g^{-1}	0.6	---	23
mesoporous $CuCo_2O_4$	1658 F g^{-1} 1 A g^{-1}	3E	5000	99% 2 A g^{-1}	0.4	---	26
mesoporous $CuCo_2O_4$	1210 F g^{-1} 2 A g^{-1}	2E, AC	5000	86% 6 A g^{-1}	1.5	42.8	28
$CuCo_2O_4$@MnO_2 CAs	416 F g^{-1} 1 A g^{-1}	2E, AG	---	---	2.0	43.3	29

double-shelled $CuCo_2O_4$	1472 F g^{-1} 4 mA cm^{-2}	2E, AC	6000	92.5% 50 mA cm^{-2}	1.5	37.3	S8
$Ni_xCo_{3-x}O_4$ nanowires	1479 F g^{-1} 1 A g^{-1}	2E, AC	3000	82.8% 20 mV s^{-1}	1.6	37.4	S9
$NiCo_2S_4$@$Ni(OH)_2$@ PPy	9.1 F cm^{-2} 5 mA cm^{-2}	2E, AC	3000	98.8% 60 mA cm^{-2}	1.6	34.7	60
$NiCo_2S_4$/Co_9S_8 hollow nanospheres	1008 F g^{-1} 1 A g^{-1}	2E, AC	3000	90% 60 mV s^{-1}	1.6	36.7	S10
$CuCo_2S_4$ nanobelt arrays	**1014 C g^{-1} at 1 A g^{-1} 1988 F g^{-1} at 1 A g^{-1} 3.88 F cm^{-2} at 1 mA cm^{-2} 1.95 C cm^{-2} at 1 mA cm^{-2}**	**2E, N-DLCHs**	**5000**	**90.89% 20 mA cm^{-2}**	**1.6**	**40.2**	**This work**

Note:3E represents three-electrode systems for single-electrode, 2E represents two-electrode systems for devices.

Table S3. The mass loading of active material in three-electrode system.

Sample	Mass loading (mg cm^{-2})
CCS-4t	2.3 ± 0.3
CCS-6t	**2.2 ± 0.3**
CCS-8t	2.1 ± 0.5
CCS-5M	2.0 ± 0.2
CCS-10M	**2.2 ± 0.3**
CCS-20M	2.1 ± 0.2
CCS-30M	1.9 ± 0.5
N-SLCHs	3.5 ± 0.5
N-DLCHs	**3.5 ± 0.5**

Table S4: Comparisons of the electrical conductivity of precursor and CCS-6t samples.

Sample	*E* (V)	*R* (Ω)	*ρ* (Ω cm)	*σ*(S/cm)	Average
CCS-6t	0.25	0.819	16.2	6.17×10^{-2}	**6.11×10^{-2}**
	0.35	0.837	16.4	6.09×10^{-2}	
	0.45	0.841	16.5	6.06×10^{-2}	
Precursor	0.25	21.81	428.5	2.33×10^{-3}	**2.35×10^{-3}**
	0.35	21.44	421.5	2.37×10^{-3}	
	0.45	21.71	426.6	2.34×10^{-3}	

Refences

(S1) Li, Zesheng, Li, Bolin, Liao, Cuina, Liu, Zhisen, Li, Dehao, Wang, Hongqiang, Li, Qingyu. One-pot construction of 3-D graphene nanosheets/Ni_3S_2 nanoparticles composite for high-performance supercapacitors. *Electrochimica Acta,* 2017, **253***,* 344-356.

(S2) C. Wang, F. Wang, Z. Liu, Y. Zhao, Y. Liu, Q. Yue, H. Zhu, Y. Deng, Y. Wu, D. Zhao. N-doped carbon hollow microspheres for metal-free quasi-solid-state full sodium-ion capacitors. *Nano Energy*, 2017, **41**, 674-680.

(S3) H. You, L. Zhang, Y. Jiang, T. Shao, M. Li, J. Bubble-supported engineering of hierarchical $CuCo_2S_4$ hollow spheres for enhanced electrochemical performance. Gong, *J. Mater. Chem. A* 2018, **6**, 5265-5270.

(S4) Y. Zhu, X. Ji, H. Chen, L. Xi, W. Gong, Y. Liu. The investigation of the electrochemically supercapacitive performances of mesoporous $CuCo_2S_4$. *RSC Adv.* 2016, **6**, 84236-84241.

(S5) J. Shen, J. Tang, P. Dong, Z. Zhang, J. Ji, R. Baines, M. Ye. Construction of three-dimensional $CuCo_2S_4$/CNT/graphene nanocomposite for high performance supercapacitors. *RSC Adv.* 2016, **6**, 13456-13460.

(S6) L.-l. Liu, K.P. Annamalai, Y.-s. Tao. A hierarchically porous $CuCo_2S_4$/graphene composite as an electrode material for supercapacitors. *New Carbon Materials*, 2016, **31** (3), 336-342.

(S7) S. Cheng, T. Shi, C. Chen, Y. Zhong, Y. Huang, X. Tao, J. Li, G. Liao, Z. Tang. Construction of porous $CuCo_2S_4$ nanorod arrays via anion exchange for high-performance asymmetric supercapacitor. *Sci. Rep.* 2017, **7**, 6681.

(S8) S. Kamari Kaverlavani, S.E. Moosavifard, A. Bakouei. Self-templated synthesis of uniform nanoporous $CuCo_2O_4$ double-shelled hollow microspheres for high-performance asymmetric supercapacitors. *Chem. Commun.* 2017, **53**, 1052-1055.

(S9) X. Wang, C. Yan, A. Sumboja, P.S. Lee. High performance porous nickel cobalt oxide nanowires for asymmetric supercapacitor. *Nano Energy*, 2014, **3**, 119-126.

(S10) Y. Shen, K. Zhang, B. Chen, F. Yang, K. Xu, X. Lu. Enhancing the electrochemical performance of nickel cobalt sulfides hollow nanospheres by structural modulation for asymmetric supercapacitors. *J. Colloid Interface Sci.* 2019, **557**, 135-143.